Centrum voor Wiskunde en Informatica
Centre for Mathematics and Computer Science

C. Nebbeling, B. Koren

An experimental-computational investigation of transonic shock wave -
turbulent boundary layer interaction in a curved test section

An Experimental-Computational Investigation of Transonic Shock Wave - Turbulent Boundary Layer Interaction in a Curved Test Section

C. Nebbeling

Delft University of Technology
Faculty of Aerospace Engineering
P.O. Box 5058, 2600 GB Delft, The Netherlands

B. Koren

Centre for Mathematics and Computer Science
Department of Numerical Mathematics
P.O. Box 4079, 1009 AB Amsterdam, The Netherlands

This paper describes an experimental investigation of a transonic shock wave-turbulent boundary layer interaction in a curved test section in which the flow has been computed by a 2-D Euler flow method. The test section has been designed such that the flow field near the shock wave at the convex wall corresponds to that near the shock wave at the upper surface of a transonic airfoil. The ratio between the radius of curvature of the wind tunnel wall and the thickness of the undisturbed boundary layer is about 80, being a mean value for modern transonic wings at cruising flight conditions. The Mach number distributions from the Euler flow computations are compared to those obtained from holographic interferometry, at flow Mach numbers upstream of the shock wave of 1.15 and 1.37. For these two Mach numbers boundary layer measurements in the interaction region have been performed by means of static pressure and pitot pressure probe traverses. Moreover extended surface pressure measurements have been made at several upstream Mach numbers M_u. In particular attention is paid to the effects of flow curvature and static pressure increase downstream of the shock wave, in relation to changing boundary layer parameters and separation phenomena.

List of symbols

c	speed of sound
c_f	skin friction coefficient
d	inner diameter
D	outer diameter
H	shape factor $(= \delta^*/\theta)$
M	Mach number
p	pressure
r	recovery factor
R	radius of curvature
Re	Reynolds number
T	temperature
u	velocity component
u_τ	friction velocity
v	velocity component
x	horizontal coordinate
y	vertical coordinate
z	crosswise coordinate
β_p	pressure gradient parameter $(= \dfrac{\theta}{u_e} \dfrac{du_e}{dx})$

2

γ	ratio of specific heats

γ ratio of specific heats
δ boundary layer thickness
δ^* boundary layer displacement thickness
θ momentum thickness
ν kinematic viscosity
ρ density

Subscripts
e   conditions at boundary layer edge
p   pitot
t   total
u   conditions just upstream of shock wave
δ conditions related to boundary layer thickness

Superscript
i   incompressible

1. INTRODUCTION

Knowledge of transonic shock wave-turbulent boundary layer interaction is crucial for the development of modern high speed aircraft wings, jet engine inlets and turbine blades. The interaction between shock wave and boundary layer has been the subject of many investigations at a variety of Mach numbers and boundary layer conditions. Often these investigations were made for boundary layers at a flat plate surface, in order to keep the amount of flow parameters as small as possible. Since the work of BRADSHAW [5], we know that streamline curvature will diminish the skin friction and enlarge the shape factor. Based on Bradshaw's findings, INGER [11] obtained by numerical investigations a reduction of the pressure gradient across the shock wave and an increase of the post-shock expansion. This led to an increase of the skin friction at the shock wave and consequently a delay of boundary layer separation at curved surfaces. Using a double-deck interaction model as Inger's, BOHNING and ZIEREP [4] obtained a decrease in pressure rise as well, by applying the Oswatitsch-Zierep pressure condition at the boundary layer edge. In spite of the undeniable influence of streamline curvature most of the recent [12, 21, 24] shock wave-boundary layer interaction research has been made at non-curved surfaces. In these the work of Schofield attracts attention by the application of a strong positive pressure gradient downstream of a shock wave-boundary layer interaction at a flat surface. A supersonic area downstream of the shock wave occurs already at an upstream Mach number M_u of 1.41, whereas without pressure gradient such a supersonic area occurs at $M_u \geqslant 1.44$.

An investigation by ALBER et al. [2] where surface curvature was considered, pointed to separation and attachment criteria for turbulent boundary layers. Since shock wave-boundary layer interaction at free flight cruising conditions takes place in general at convex walls, the present investigation concentrates, as opposed to Alber, on shock wave-boundary layer interaction where a local transonic flow area is followed by a curved normal shock wave. To obtain a quantitative description of the flow field near the interaction zone, surface pressure and probe pressure measurements were made. During the measurements the shock position was kept fixed by a far downstream, computer controlled choke mechanism which used a static pressure difference across the shock wave as input parameter. The tests, which were made at upstream Mach numbers of 1.15 and 1.37, confirm the strong influence of surface curvature on the shock wave-turbulent boundary layer interaction. For both Mach numbers, the complete inviscid flow field in this wind tunnel section has been computed by an Euler flow method [13].

2. THE CURVED TEST SECTION

The experiments were performed in a curved two-dimensional test section of the ST15 blow-down wind tunnel at the Faculty of Aerospace Engineering of the Delft University of Technology. The test section is 150 mm wide and about 165 mm high. The air supply of the wind tunnel consists of a 300 m^3 vessel containing air at an initial pressure of 40 Bar. Dependent on the total pressure of the flow in the wind tunnel the run-time may be about 25 minutes. The temperature drop in the vessel is compensated for by a heat capacity consisting of 20 tons of ceramic marbles. The test section was designed such that the ratio of surface curvature and boundary layer thickness, $(R/\delta)_u$, corresponds to free flight conditions. According to INGER [11] a value between 50 and 100 might fulfill this requirement. For the present design $(R/\delta)_u = 80$ has been the option. Since the expected boundary layer thickness near the shock wave was about 5.5 mm the actual radius of curvature of the convex lower wall was chosen equal to $R = 450$ mm. The height of the test section followed from the condition that at a lower wall Mach number of 1.45 the Mach number at the (concave) upper wall of the test section should be less than $M = 0.85$ [17]. This led to a test section height of about 165 mm. The entire transonic test section has been designed within the constraints of the wind tunnel structure, i.e. the distance between settling chamber and diffuser, the position of the side-windows and the vertical distance between the liners. The total design was pointed to a continuous static pressure decrease at the lower wind tunnel wall up to a minimum near the shock wave. The final design is given in Fig. 1.
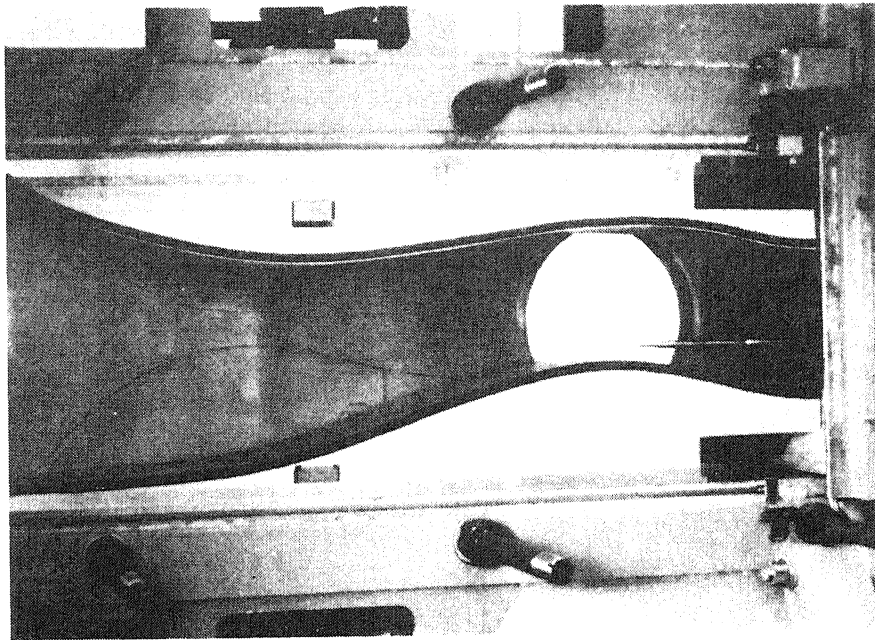

Fig. 1. Curved test section in opened wind tunnel.

In order to judge about the need of side-wall boundary layer fences surface flow visualizations have been made of the convex curved boundary layer flow at $M_u = 1.15$ and $M_u = 1.37$. Since the flow showed a reasonable amount of two-dimensionality near the plane of symmetry, priority was given to the application of optical techniques, and side-wall fences were not applied. To ensure adiabatic wall conditions the convex curved nozzle block has been constructed out of wood, clad with a 0.4 mm thick layer of phosphorus bronze, in which the surface pressure taps were drilled. The bronze cover allowed for an electrical signal, indicating the starting position for the traversing boundary layer probes.

3. EULER FLOW SOLUTIONS

3.1. Discretization and solution method

The steady 2-D Euler equations can be written on the domain $\Omega \subset \mathbb{R}^2$ as

$$\frac{\partial f(q)}{\partial x} + \frac{\partial g(q)}{\partial y} = 0, \quad \text{with} \tag{1}$$

$$q = \begin{bmatrix} \rho \\ \rho u \\ \rho v \\ \rho e \end{bmatrix}, \quad f = \begin{bmatrix} \rho u \\ \rho u^2 + p \\ \rho u v \\ \rho u(e + \frac{p}{\rho}) \end{bmatrix}, \quad g = \begin{bmatrix} \rho v \\ \rho v u \\ \rho v^2 + p \\ \rho v(e + \frac{p}{\rho}) \end{bmatrix}, \quad \text{and} \tag{2}$$

$$e = \frac{1}{\gamma - 1} \frac{p}{\rho} + \frac{1}{2}(u^2 + v^2). \tag{3}$$

The Euler equations are discretized in their integral form

$$\int_{\partial \Omega^*} (f n_x + g n_y) ds = 0. \tag{4}$$

With $\delta \Omega^*$ we denote the boundary of an arbitrary subregion $\Omega^* \subset \Omega$, and with n_x and n_y the components of the outward unit normal along $\delta \Omega^*$. A simple way to discretize (4) is to subdivide Ω into disjoint quadrilateral subregions Ω_{ij} (finite volumes), and to assume that the flux functions f and g are constant along each volume wall. This gives the following discretization:

$$\sum_{k=1}^{4} \{f(q^l_{ij,k}, q^r_{ij,k}) n_{x_{ij,k}} + g(q^l_{ij,k}, q^r_{ij,k}) n_{y_{ij,k}}\} s_{ij,k} = 0, \quad \text{for all } ij, \tag{5}$$

in which the subscript k refers to the kth wall of the quadrilateral volume Ω_{ij}, and the superscripts l and r to the left and right side of this wall respectively.

For the Euler equations, because of their rotational invariance, (5) may be further simplified to

$$\sum_{k=1}^{4} T^{-1}_{ij,k} f(T_{ij,k} q^l_{ij,k}, T_{ij,k} q^r_{ij,k}) s_{ij,k} = 0, \quad \text{for all } ij, \text{ with} \tag{6}$$

$$T_{ij,k} = \begin{bmatrix} 1 & 0 & 0 & 0 \\ 0 & n_{x_{ij,k}} & n_{y_{ij,k}} & 0 \\ 0 & -n_{y_{ij,k}} & n_{x_{ij,k}} & 0 \\ 0 & 0 & 0 & 1 \end{bmatrix} \tag{7}$$

In each volume, the state is assumed to be an approximation of the mean value of the exact solution. The states $q^l_{ij,k}$ and $q^r_{ij,k}$ are simply taken equal to the state in volume Ω_{ij}, respectively the state in the neighbouring volume $\Omega_{ij,k}$. This yields the first-order accurate discretization

$$\sum_{k=1}^{4} T^{-1}_{ij,k} f(T_{ij,k} q_{ij}, T_{ij,k} q_{ij,k}) s_{ij,k} = 0, \quad \text{for all } ij, \tag{8}$$

in which $q_{ij,k}$ denotes the state in $\Omega_{ij,k}$.

For the evaluation of the flux vector f at the volume walls, the flow at each volume wall is considered as the local solution of the 1-D Riemann problem for the two gas states q_{ij} and $q_{ij,k}$. For the solution of the 1-D Riemann-problem, the approximate Riemann solver as proposed by OSHER [18] has been chosen. The choice for Osher's scheme is motivated among others by: (i) its consistent treatment of boundary conditions, and particularly (ii) its suitability for Newton-type solution techniques.

To solve the non-linear system (8) point (= volume) relaxation methods were considered, in which one or more local Newton steps are used for the collective relaxation of the 4 unknowns in each single volume. The most efficient relaxation is obtained by selecting a large tolerance for the Newton iteration, so that in all but exceptional cases only a single Newton step is taken. These relaxation methods are simple and robust, but need an acceleration. When one uses collective symmetric Gauss-Seidel as a point relaxation method, a suitable acceleration technique is found in multigrid. As a very efficient and robust multigrid technique, use is made of: non-linear multigrid preceded by nested iteration, in order to obtain a good initial estimate [8, 9].

3.2. Grid generation and adaptation

In order to obtain a good resolution of large local gradients (which are decided to be important), and yet not to have high computational costs, locally refined grids are used. In order not to lose the order of accuracy of the discretization, the refinements are smooth.

For the computational results presented hereafter, we used grids with stretching, as shown (for a 4-level multigrid strategy) in Fig. 2.
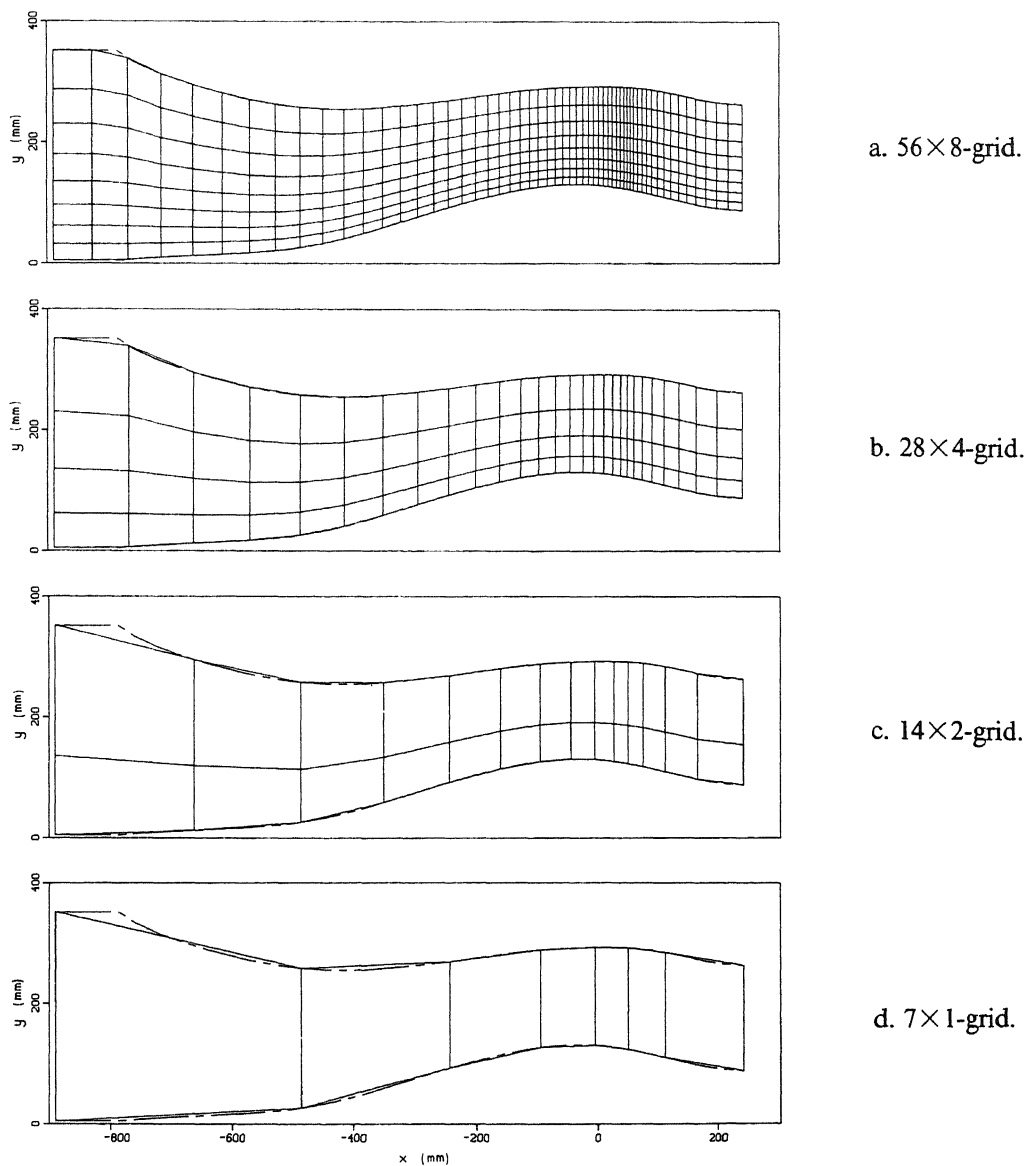
a. 56×8-grid.

b. 28×4-grid.

c. 14×2-grid.

d. 7×1-grid.

Fig. 2. Family of grids for test section.

The dashed lines in Fig. 2 indicate the lower and upper wall. The stretching in x-direction is such that the grids are finest at the foot of the shock wave. In the solution process, initially the x-location of this fine region is taken equal to the x-location of the wind tunnel throat. The location is adapted during the nested iteration. The grid adaptation works in the following way: after each solution prolongation in the nested iteration phase, we search for the x-solution of the maximum velocity gradient at the lower wall, downstream of the throat, and define this location as the x-location of the foot of the possible shock wave. Hereafter, we generate the new grids. Without any correction, the states q_{ij} are shifted together with the volumes Ω_{ij}. Doing this the quality of the finest grid solution as yielded by the nested iteration becomes worse. However, no significant deterioration of convergence rates has been observed. For a detailed description of the grid generation and adaptation, we refer to [13].

3.3. Boundary conditions at in- and outlet

The inlet flow has been prescribed to be subsonic, so requiring three boundary conditions. Constant values $u = u_{inlet}$, $v = 0$, $c = c_{inlet}$ have been chosen, with c denoting the speed of sound ($= \sqrt{\gamma p / \rho}$). The choice of constant values was motivated by the fact that the inlet is flat and parallel.

The outlet flow is subsonic as well, so requiring one boundary condition. Because of the fact that the outlet part is non-flat and non-parallel, the outlet boundary condition cannot be as trivial as those at the inlet. The following possibility has been considered: $p = p(y)$, as solution of the equation of curvilinear motion

$$\frac{dp(y)}{dy} = \gamma \frac{p(y) M_{outlet}^2}{R(y)} \cos(\phi(y)),$$

(9)

with $R(y)$ the distribution of the radii of curvature of the streamlines, and $\phi(y)$ the distribution of the angles between the streamlines and the x-axis. For $1/R(y)$ and $\phi(y)$ linear distributions have been used, such that they fitted the channel outlet. M_{outlet} has been determined with the 1-D flow theory. Using the 1-D flow theory value of p as value for p at the lower wall, an initial value problem was obtained. The initial value problem has been solved by means of a Runge-Kutta-Merson method.

3.4. Numerical results

Computational results obtained for $M_u = 1.15$ and $M_u = 1.37$ are shown in Fig. 3a resp. 3b. The markers in all surface distributions correspond to volume wall centres; the square to those at the lower surface and the circular to those at the upper surface.

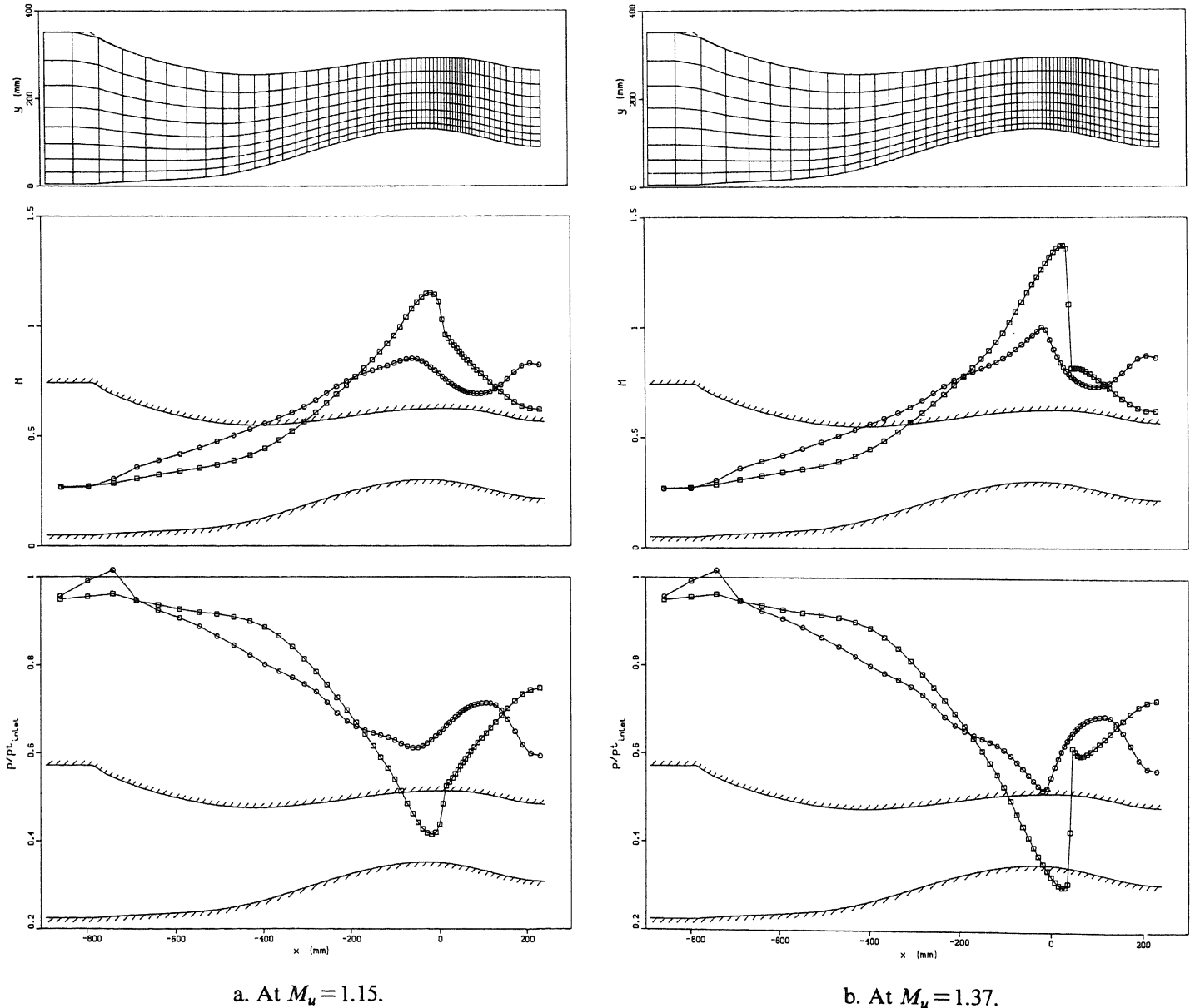a. At $M_u = 1.15$.

b. At $M_u = 1.37$.

Fig. 3. Numerical results.

From the finest grids and surface distributions obtained, it can be seen that for both flows the grid adaptation is good.

Clearly visible for $M_u = 1.37$ is the occurrence of an after-expansion. Since a first-order accurate Osher-type discretization yields solutions without spurious non-monotonicity, the after-expansion occurring for $M_u = 1.37$ is not a numerical artefact, but a correct part of the Euler flow solution indeed.

3.5. Comparison with holographic interferometry results

The interferometrical and numerical results (Fig. 4) show a perfect quantitative agreement away (of course) from the wall and shock wave.
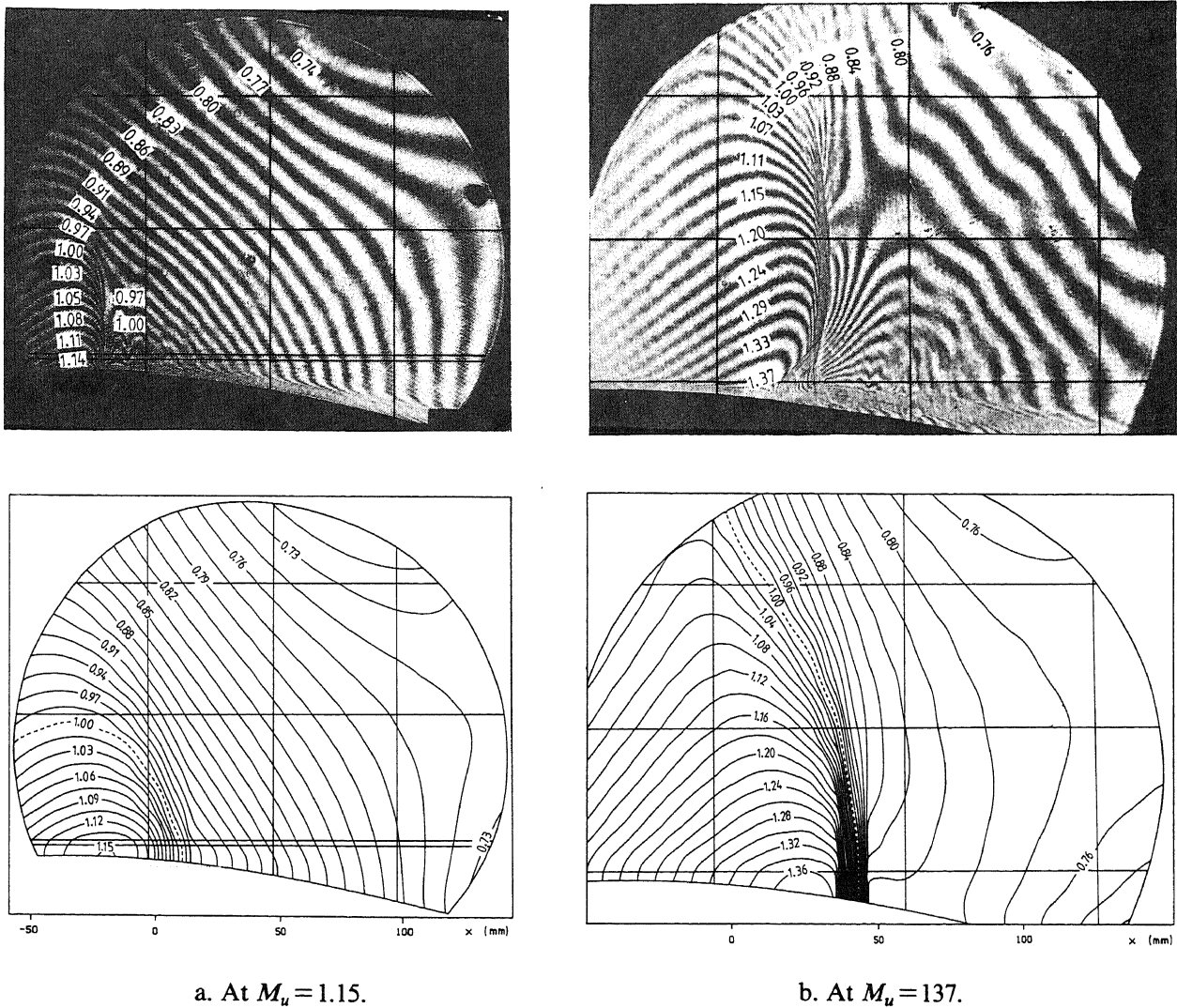

a. At $M_u = 1.15$.

b. At $M_u = 137$.

Fig. 4. Interferometrical and numerical Mach number distributions.

The differences between both results can be exploited. Given an Euler code which has proved to be reliable, its results can be considered confidently as experimental results with viscosity and heat conduction switched off. Its results can be used to pick out from experimental results: simple viscous phenomena and, in particular, complicated viscous-inviscid phenomena. The present Euler code has proved to be reliable [10, 14, 15]. Here, its results learn us for instance that the downstream supersonic pocket (at both $M_u = 1.15$ and $M_u = 1.37$) and the λ-shock (at $M_u = 1.37$) are viscous-inviscid phenomena indeed, and that due to viscous effects the shock wave has been pushed slightly upstream (at both $M_u = 1.15$ and $M_u = 1.37$).

4. EXPERIMENTAL TECHNIQUES

The experiments were made (i) at a total pressure of 1.65 Bar, a total temperature of about 270 K and an upstream Mach number of 1.15, and (ii) at a similar total temperature, a total pressure of 1.8 Bar and an upstream Mach number of 1.37. The specific Reynolds numbers were $Re = 2.7 \; 10^7 \; m^{-1}$ at $M_u = 1.15$ and $Re = 2.9 \; 10^7 \; m^{-1}$ at $M_u = 1.37$. Related to the measured boundary layer thickness just in front of the shock wave the Reynolds number appeared to be $Re_\delta = 1.2 \; 10^5$ for both flow conditions. The flow measurements were mainly restricted to pitot and static pressure probe traverses through the boundary layer, and to static surface pressure measurements. Most of the traverses were made with a computer controlled probe support downstream of the choke section. At about 250 mm upstream of the shock wave, a boundary layer probe with 0.3 mm outer diameter, passing through the wall surface, was used to measure the undisturbed boundary layer profile far upstream of the interaction. The step size of this probe was about 0.1 mm. For the pitot probe near the shock wave, a step size of about 0.2 mm was applied close to the surface, and a step size of about 1.2 mm at normal distances exceeding 4 mm. Because of the small normal static pressure gradient, the step sizes for the static probe were 1 mm and 2 mm dependent on the distance from the surface. Since the velocity of the inviscid outer flow decreases continuously with increasing distance from the convex wall, the boundary layer edge has been taken there where the velocity reaches its maximum value. To obtain velocity profiles in the boundary layer the Mach number distribution was determined from the measured static and pitot pressures. Assuming constant total temperature a first approximation for the temperature and velocity profile was made. Further approximations for these profiles were made with Crocco's formula

$$\frac{T}{T_e} = 1 + r\frac{\gamma - 1}{2}M_e^2\{1 - (\frac{u}{u_e})^2\}, \tag{10}$$

with $r = 0.89$, the recovery factor for turbulent boundary layers at an adiabatic wall. At each station three iteration cycles were made to obtain a steady solution for the temperature and velocity profile. During the investigations the following probes were used:

(i) a boundary layer probe 250 mm upstream of the shock wave ($D = 0.3 \; mm$, $d = 0.18 \; mm$),

(ii) a pitot probe upstream of the shock wave ($D = 0.4 \; mm$, $d = 0.25 \; mm$),

(iii) a pitot probe downstream of the shock wave ($D = 0.7 \; mm$, $d = 0.4 \; mm$) and

(iv) a static pressure probe ($D = 1 \; mm$, pressure taps $d = 0.3 \; mm$).

For the latter probe four static pressure taps were applied at 30° with respect to the plane of symmetry of the flow to diminish cross-flow influence. At the pitot probe measurements, a displacement correction of $0.15D$ has been applied. The pitot probes were also used as Preston probes to provide the local skin friction coefficients. Schlieren and shadow pictures have been made to get an overall impression of the flow field. Holographic interferometry allowed the determination of scalar quantities such as temperature and density.

5. BOUNDARY LAYER MEASUREMENTS

5.1. Surface pressure distribution

Preceeding to the boundary layer measurements, the flow downstream of the shock wave was examined for two-dimensionality in two different ways. First, surface flow visualization was applied with a mixture of China clay, titanium-dioxide and oil. Thereafter, some pitot probe traverses were made at the plane of symmetry and at 25% of the tunnel width. Neither the surface flow visualization nor the pitot probe traverses show a severe lack of two-dimensionality at an upstream Mach number of 1.15. At a Mach number of 1.37 three-dimensional effects were observed in both the pitot pressure distributions and the surface flow visualizations. For the latter Mach number Fig. 5 shows the separation bubble downstream of the shock wave. This figure clearly indicates that only a small centre part consists of a more or less parallel surface flow. The pitot pressure distributions of Fig. 6 show large differences near the wall but do coincide at normal distances exceeding 20 mm. Most embarassing is Fig. 7 in which (for $M_u = 1.37$) a surface flow pattern is shown with the static pressure probe touching the wall surface, and inducing a really two-dimensional surface flow. Considering the measurements, this phenomenon must be kept in mind.
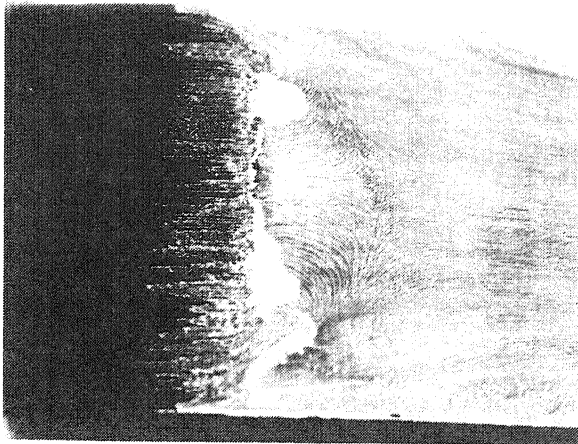
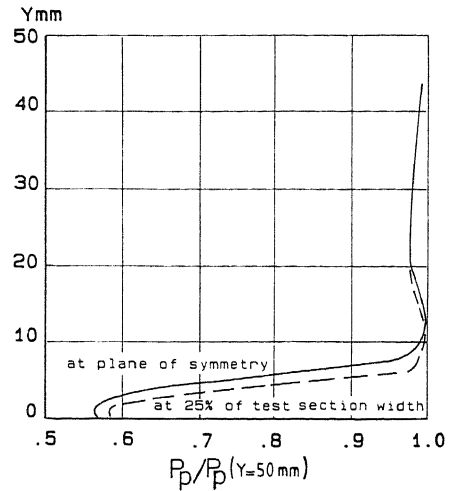9

Fig. 5. Surface flow pattern at $M_u = 1.37$.

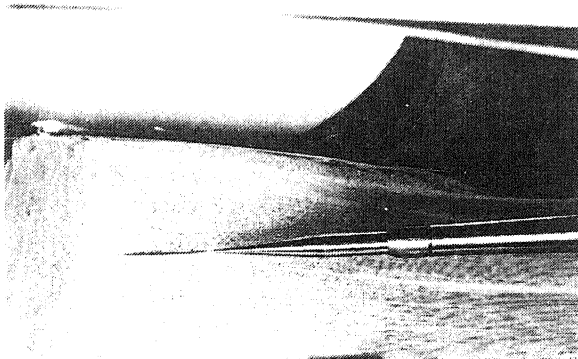Fig. 6. Pitot pressure distribution 42 mm upstream of shock wave, at $M_u = 1.37$.

Fig. 7. Surface flow pattern with pressure probe touching the surface, at $M_u = 1.37$.

Preceeding to the boundary layer measurements surface pressure distributions have been measured in the plane of symmetry at upstream Mach numbers ranging from $M_u = 1.03$ up to $M_u = 1.37$, including $M_u = 1.15$. These measurements at flow conditions not disturbed by probes provide a check of the accuracy of the static pressure probe measurements close to the wall. The general tendency of the obtained surface pressure distributions is a pressure decrease in downstream direction down to a minimum value, followed by a more or less steep pressure rise depending on the strength of the shock wave (Fig. 8).
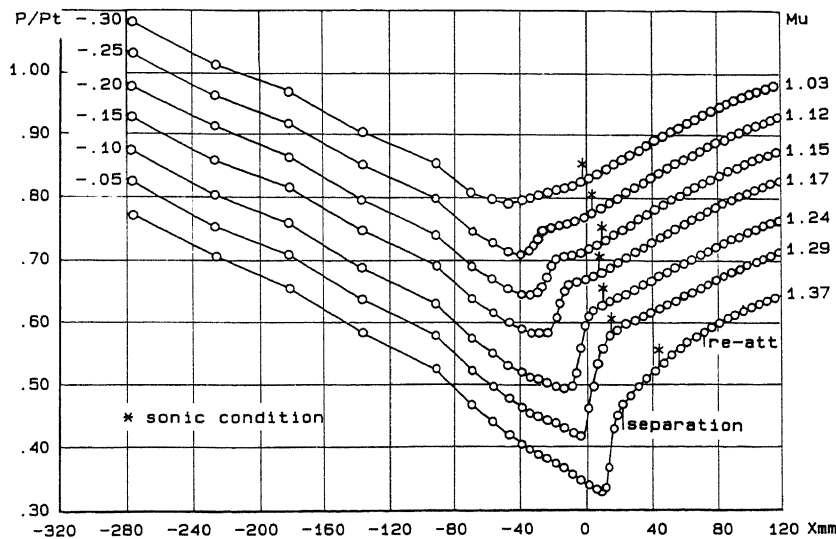

Fig. 8. Surface pressure distribution at different upstream Mach numbers.

Most of the pressure distributions have in common that this steep pressure rise stops abruptly, and is followed by a less steep pressure increase, a phenomenon frequently observed at shock wave-boundary layer interactions. Peculiar in the present results is the change in pressure increase at a pressure level far below the local sonic pressure. In literature most investigations indicate this change in pressure gradient near or above the sonic pressure [1, 2, 7]. Only at very high Reynolds numbers a similar behaviour of the wall pressure distribution has been found [19, 22, 24]. A comparison with the results of SCHOFIELD [21] seems to exclude the high downstream pressure gradient as a reason. Since the results in [1] show a downstream plateau pressure as well, the shock strength and (at lower Mach numbers) the surface curvature will certainly play a role. For flat plate boundary layers PADOVA et al. [19] also found abrupt changes in pressure gradient at pressure levels below the sonic wall pressure. These changes could be correlated to the bifurcation height of their shock wave. Since in the present experiments the shock wave was not bifurcated at the lower Mach numbers, surface curvature is expected to be the main cause. The much higher values at which the plateau pressures at curved surfaces arise in [6, 16], are probably caused by the non-smooth downstream joining of the convex hump and the flat wind tunnel wall. At higher Mach numbers a decrease in pressure gradient occurs at flat surfaces in the case of flow separation, as measured by SEDDON [22]. This decrease corresponds to the present (curved wall) measurements at higher Mach numbers. However, in the present results, this decrease at higher Mach numbers is much smaller than that at lower Mach numbers, which meets the results of ALBER et al. [2].

5.2. Normal static pressure distribution

Normal static pressure distributions have been measured upstream and downstream of the shock wave at $M_u = 1.15$ and $M_u = 1.37$. Traverses have been made (i) from 40 mm upstream of the shock wave up to 70 mm downstream at $M_u = 1.15$, and (ii) from 45 mm upstream to 60 mm downstream at $M_u = 1.37$. The pressures have been measured with a 0.5 mm step size at the first 10 mm above the surface and with a 1.2 mm step size further above. At $M_u = 1.37$, no differences in upstream static pressure distribution could be observed between the measurements at the plane of symmetry and those at 25% of the tunnel width. Downstream of the shock wave the differences are remarkable (Fig. 9).
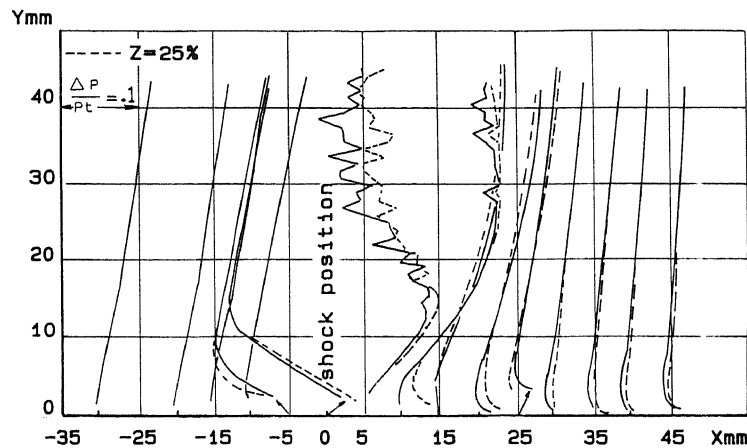

Fig. 9. Normal static pressure distribution w.r.t. wall static pressure
at $z = 50\%$ and $z = 25\%$, at $M_u = 1.37$.

No static pressure traverses were made at 250 mm upstream of the shock wave. Since the local flow curvature is small, the static pressure in the boundary layer over there was considered to be the measured surface pressure. In general the static pressure probe measurements near the surface agree fairly well with the measured surface pressures. Only near the shock wave large differences occur. At the data reduction to velocity profiles special attention must be paid to this. Outside of the shock wave region the normal pressure distributions are linear, which was the option of the wind tunnel design.

5.3. Normal pitot pressure distributions

Pitot pressure traverses have been made at 250 mm upstream of the shock wave and at locations corresponding to the static pressure traverses. The pitot pressures have been measured at each 0.18 mm from the wall, but at distances exceeding 4 mm at each 1.2 mm a measurement was made. The pitot pressure distributions at $M_u = 1.15$ show some influence of the shock wave and the downstream pressure gradient. At $M_u = 1.37$ the pitot pressure distributions are much more influenced by the shock wave, but also by the downstream separation (Fig. 6).

To get a better understanding of the flow structure, Mach number and velocity distributions have been determined.

5.4. Mach number and velocity profiles

At $M_u = 1.15$ the Mach number distribution in the boundary layer has been determined from the pitot and static pressure traverses. Near the wall a linear interpolation was applied between the wall static pressure and the nearest data point of the normal static pressure traverses. Near the shock wave, where the probe static pressures differ considerably from the wall static pressures, the latter have been used. (The probe measurements are assumed to be unreliable over there.) At $M_u = 1.37$ the Mach number distribution upstream of the shock wave has been computed in the same way as for $M_u = 1.15$. Downstream of the shock, where a flow separation occurred, a different procedure was chosen. Since the probe influenced the separated flow region in an unconfined way the reliability of the traversing probe results is questionable. The greater part of the measured pressure distributions shows a decreasing static pressure towards the wall with a distinct minimum value at some distance from the surface, followed by a further static pressure increase (Fig. 10).
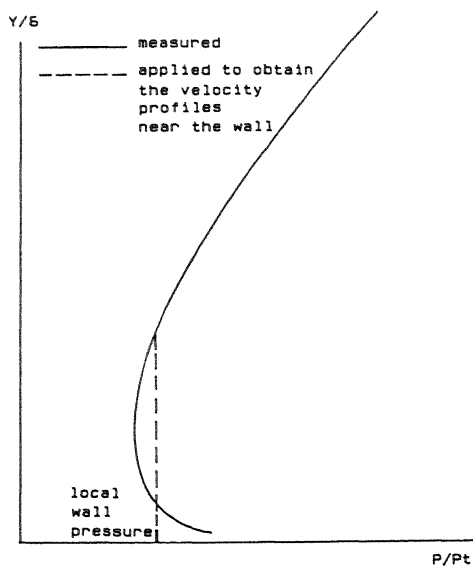

Fig. 10. Schematic static pressure distribution normal to the wall, downstream of the shock wave.

This pressure distribution is most unlikely and has to be attributed to a change in flow structure during the probe traverse. To determine the Mach number distribution in this area the static pressure has been taken identical to the measured static wall pressure up to a normal distance where the measured probe static pressure exceeds the local surface static pressure (Fig. 10). Next the velocity distributions were calculated using the settling chamber temperature and applying the Crocco relation for a turbulent boundary layer along an adiabatic wall. The velocity profiles, non-dimensionalized by the boundary layer edge velocity, are given in Fig. 11.
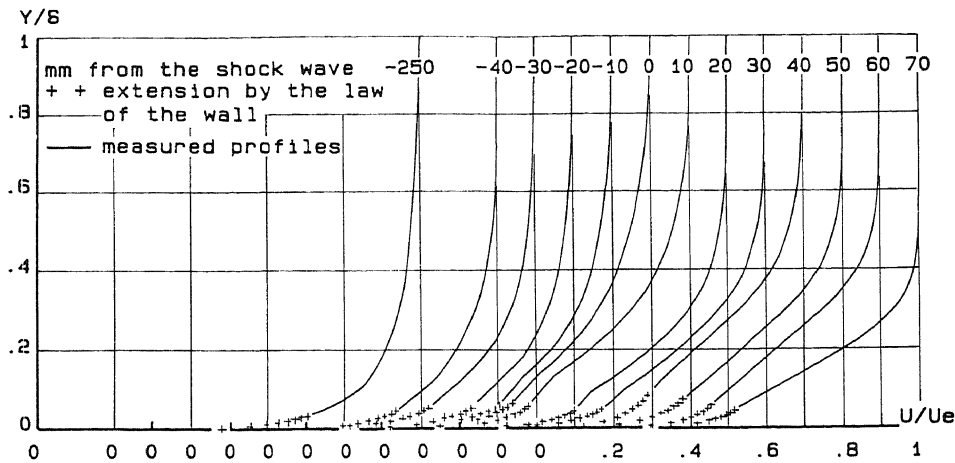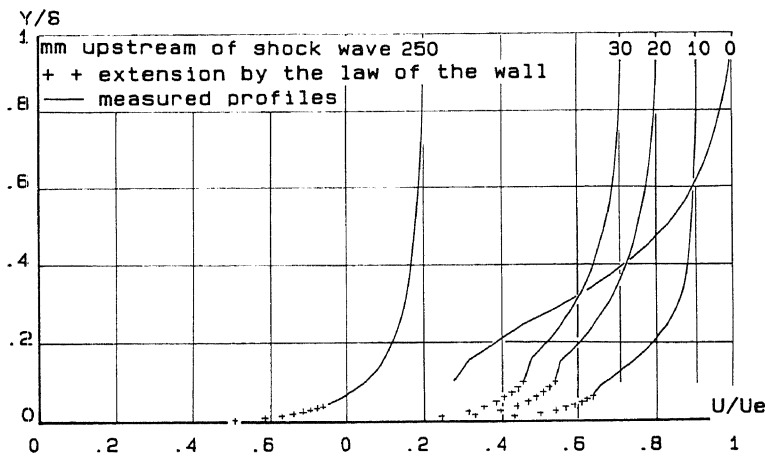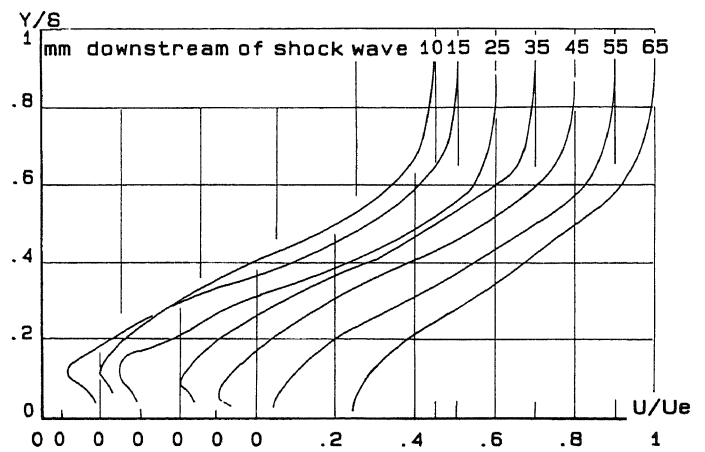
a. At $M_u = 1.15$.

b1. Upstream of shock wave, at $M_u = 1.37$.

b2. Downstream of shock wave, at $M_u = 1.37$.

Fig. 11. Velocity profiles.

To determine the boundary layer integral parameters the regular turbulent boundary layer profiles are extrapolated to the surface by means of the law of the wall in the compressible form of WINTER and GAUDET [25]:

$$\frac{u}{u_\tau^i} = 6.05 \log\frac{yu_\tau^i}{\nu_e} + 4.05 \tag{11}$$

The incompressible friction velocity u_τ^i has been obtained by using the measured velocity nearest to the surface. Because of the severe shock-induced change of the regular turbulent boundary layer profile at $M_u = 1.37$, no extrapolations have been applied downstream of this shock wave.

5.5. Skin friction distribution and flow separation

The skin friction distributions have been determined from Preston probe measurements as well as from Clauser plots. As far as the Preston probe measurements are concerned, the calibrations of PATEL [20] have been applied and have been corrected for compressibility effects by means of the reference temperature hypothesis. Since the compressibility corrections of ALLEN [3] led to more consistent results than those of SIGALLA [23], preference is given to Allen's functions. From the Clauser plots the skin friction distributions were determined graphically for each measured velocity profile. The results from Preston probe measurements and Clauser plots are given in Fig. 12 for both $M_u = 1.15$ and $M_u = 1.37$.
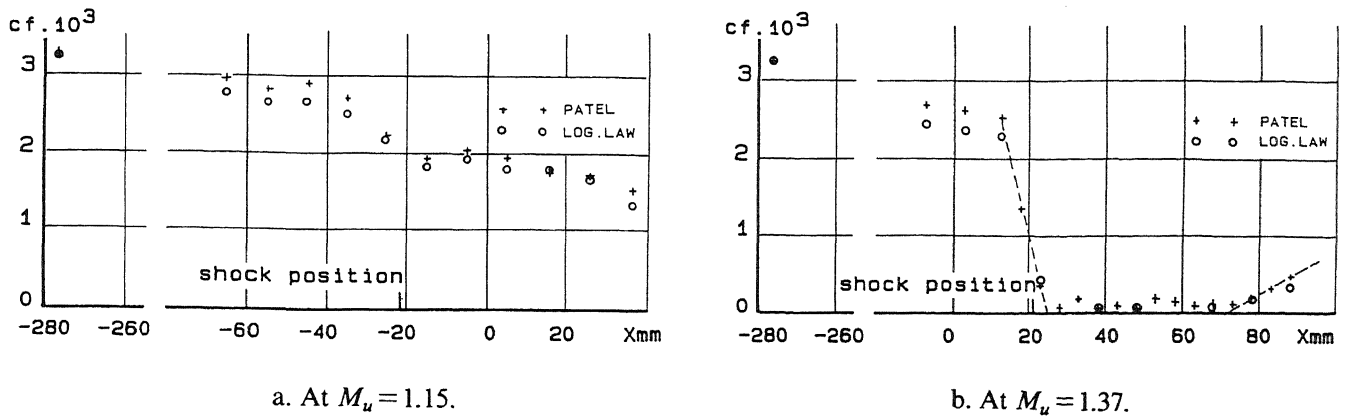
a. At $M_u = 1.15$.   b. At $M_u = 1.37$.

Fig. 12. Wall shear stress distribution.

In general the skin friction values obtained from Patel's equations exceed those from the Clauser plots. This difference might be attributed to a difference in allowance for compressibility, since the Winter and Gaudet correction $c'_f = \sqrt{1 + 0.2 M_e^2}\ c_f$ has been applied at the Clauser plot results. For $M_u = 1.15$ the skin friction decreases about 30% near the shock wave followed by a slight recovery after which a continuous reduction by the adverse pressure gradient starts without leading however to a flow separation in the considered region. For $M_u = 1.37$ the skin friction distribution in downstream direction is quite different. Near the shock wave a steep reduction to a "zero" value occurs. This value persists for about 50 mm after which a gradual increase in the skin friction occurs. Because of differences in the determination of the skin friction, the downstream location where the skin friction starts to increase is not self-evident. However, the skin friction measurements from the Clauser plots will not be very reliable, since a well-developed turbulent boundary layer cannot be expected just downstream of the re-attachment point. In that region the Preston probe measurements will be more reliable and an extrapolation of the last three data points leads to a well-defined re-attachment point 46 mm downstream of the separation point. A comparison with the oil flow visualization technique indicates a shorter separated region. Here the separation length does not exceed a length of 39 mm, which corresponds well with the Clauser plot results. The reason for this has been given before. As soon as the pressure probe touches the surface the structure of the separated region will change as shown by the oil flow patterns. This might explain why all measured skin friction values are positive in the separated region, independent whether the Clauser plots were used near re-attachment, or Patel's equations in the whole separated region. Nevertheless, the Clauser plots seem to yield the most reliable results in this region of re-attached flow.

5.6. Separation and re-attachment

Criteria for separation and re-attachment in transonic flow have been studied by ALBER et al. [2]. These investigations yielded the following description for shock- and pressure-induced separation of a turbulent boundary layer. At an upstream Mach number below $M_u = 1.32$ a gradual compression up to the sonic wall pressure preceeds flow separation, whereas at $M_u > 1.32$ a Prandtl-Meyer-type compression of 6.6° occurs before separation. The latter one is characterized by shock-induced separation, whereas compressions requiring a flow deflection smaller than 6.6.° are characterized by pressure-induced separations. In this regime flow separation seems to be governed by a pressure gradient parameter β_p. At pressure-induced separation ALBER et al. found this parameter to be about 0.004, whereas shock-induced separation occurred at the maximum value of β_p. Re-attachment was found for both separation phenomena at about equal values of β_p, being $\beta_p \approx 0.0065$.

For the present investigation the shock-induced separation at $M_u = 1.37$ was observed indeed at the maximum value of β_p (Fig. 13), but at re-attachment the value of β_p was only 0.0035, which is lower than the value given by ALBER et al.
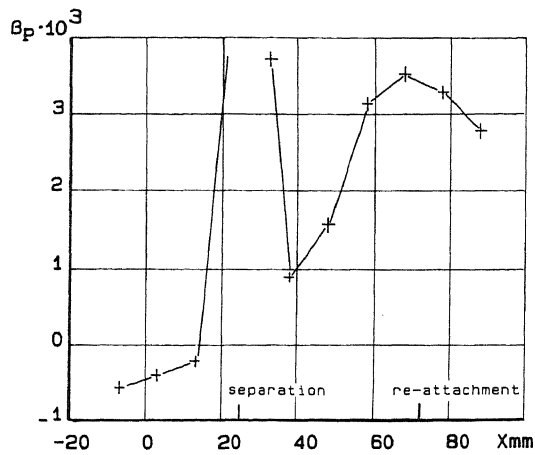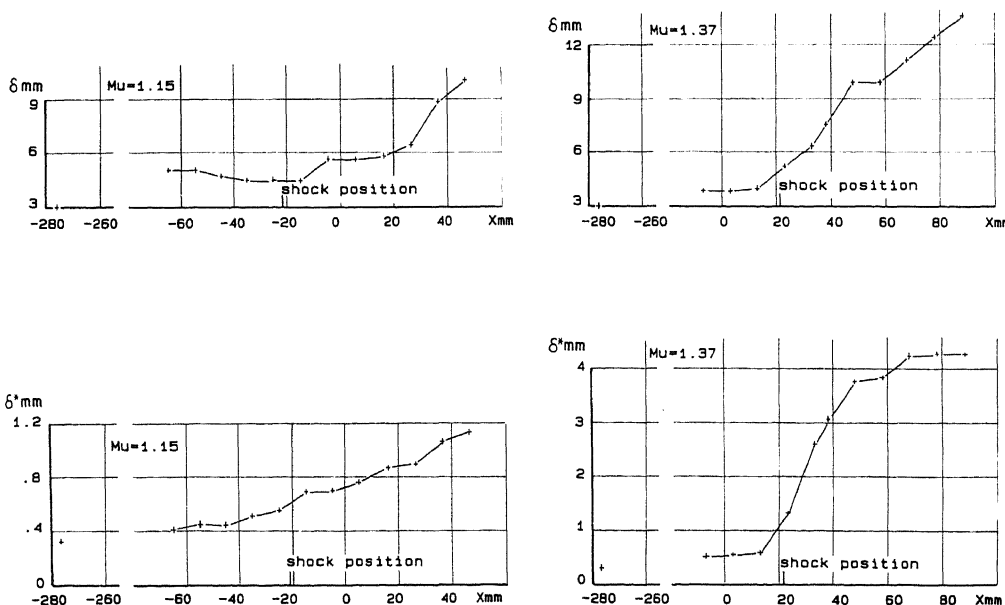
Fig. 13. Pressure gradient parameter distribution.

Certainly, there exists resemblance between the experimental set-up of ALBER et al. and the present set-up, but an obvious difference is the wall contour downstream of the shock wave. In Alber's experiment re-attachment occurred at the flat surface downstream of the hump, as at the present experiments re-attachment occurred at the convex part of the curved wall. This might be the cause of the difference in β_p at the re-attachment point, the more so as for both experiments the pressure gradient in the separated region is about 1.2 Bar/m.

5.7. Boundary layer thickness and integral parameters

The boundary layer thickness δ, the integral parameters δ^* and θ, and the shape factor H have been given in Fig. 14 for both $M_u = 1.15$ and $M_u = 1.37$, where the Reynolds numbers related to the shock positions are: Re=2.0 10^7 respectively 2.3 10^7, and related to the boundary layer thickness: Re$_\delta$ = 1.2 10^5 for both flows. Because of the small difference in the main flow Reynolds numbers, the difference in boundary layer thickness must be imputed to differences in pressure gradients of the main flow upstream. For $M_u = 1.37$ a substantial growth of the boundary layer occurs downstream of the shock wave. For $M_u = 1.15$ the boundary layer seems to be unaffected for a while.

a. Boundary layer thickness.

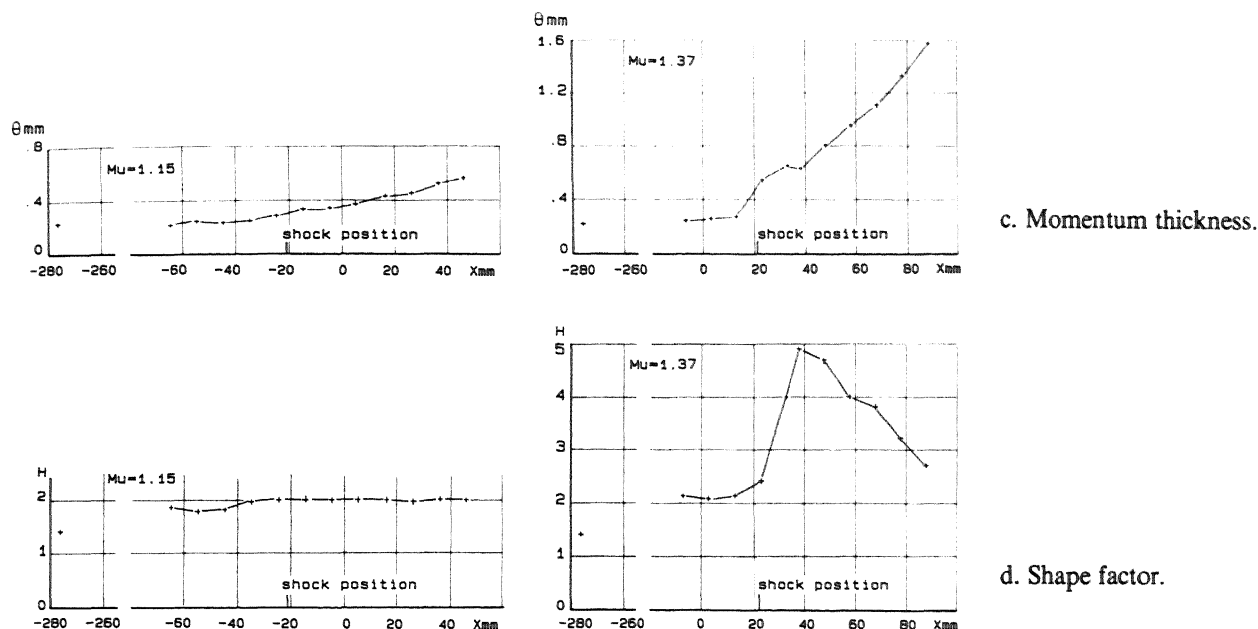b. Boundary layer displacement thickness.

c. Momentum thickness.

d. Shape factor.

Fig. 14. Distribution of boundary layer thickness and integral parameters.

However, from Fig. 14 it appears that the displacement thickness δ^* and the momentum thickness θ are affected immediately by the shock wave, even at the lower upstream Mach number. At $M_u = 1.37$ the increase of the displacement thickness δ^* is about 8 times the upstream value, which is far in excess of the factor 4.5 in Kooi's experiment at a Mach number of 1.4. The difference must be attributed to the adverse pressure gradient in the present measurements. This is sustained by the experiments of Schofield, where with $M_u = 1.41$, Re $= 3.7 \ 10^6$ and a strong adverse pressure gradient, a factor 8.5 was found. At $M_u = 1.15$, δ^* increases only with a factor 1.55 in spite of the adverse pressure gradient which is still considerable.

For $M_u = 1.37$ the momentum thickness θ increases through the shock wave from 0.26 mm to 0.66 mm near the point of separation. Reaching the point of re-attachment, θ has increased up to 1 mm and increases still further downstream. So the growth through the shock wave is a factor 2.5 and at the re-attachment point the total growth factor is 3.8. Far downstream of the shock wave Kooi reaches a factor of 3.2, with $M_u = 1.4$ and without a downstream pressure gradient. At $M_u = 1.15$ the growth factor for the momentum thickness is about 1.4 which is rather high compared to the results of GADD [7].

To judge about the condition of the boundary layer the shape factor $H = \delta^*/\theta$ will be considered. At $M_u = 1.15$, H increases from the undisturbed value 1.8 to 2 near the shock wave. This increase is mainly caused by the surface curvature, since at normal flat plate interaction at this Mach number hardly any increase in shape factor has been observed. At $M_u = 1.37$ the shape factor measured at the interaction region corresponds to the results of Kooi, Seddon and Schofield at strong interactions. In a region of increasing shape factor, separation of the boundary layer is generally found where H reaches the value 2.6. The present investigation confirms this finding. No influence has been observed of the surface curvature or the adverse pressure gradient on the shape factor at separation. Downstream of separation H increases up to a maximum value of 4.9, which is much higher than the maximum value of 3.5 measured by Kooi. Based on numerical computations Inger obtained indications about an increase of the shape factor owing to surface curvature and a downstream adverse pressure gradient. In the present results H decreases within a rather short distance to a value which is comparable to the undisturbed upstream value. At a non-curved surface and with an adverse pressure gradient similar to that of the present measurements, Schofield has measured at $M_u = 1.41$ a maximum value of $H = 10.2$, the Reynolds number related to the shock position being 3.7 10^6, i.e. 5 times less than in the present measurements. This implies a major effect of the adverse pressure gradient and the Reynolds number on the shape factor of the boundary layer downstream of the shock wave.

6. CONCLUSIONS

The utility of a reliable Euler code in research on viscous-inviscid interactions may be twofold. It may be used (i) as a tool for designing (and re-designing) an experimental set-up, and (ii) as a tool for understanding complicated experimental results. The latter use does not seem to be important in present-day research. However, given the recent availability of very reliable (and moreover very efficient) Euler codes, this use might become of paramount importance in near-future research.

A shock wave-boundary layer interaction at a convex curved surface has been investigated experimentally at upstream Mach numbers of $M_u = 1.15$ and $M_u = 1.37$. At both Mach numbers the stream-line curvature leads to a supersonic region downstream of the shock wave. Relying on the Euler flow computations this must be attributed to viscous effects.

Surface curvature and the adverse pressure gradient induce, compared to flat plate experiments without adverse pressure gradient, an increase of the boundary layer displacement thickness and of the shape factor.

No increase of the separation length has been measured with respect to experiments at non-curved surfaces.

The separation criterium of ALBER et al. agrees with the present findings, this does not apply to the re-attachment criterium.

ACKNOWLEDGEMENT

REFERENCES

1. J. ACKERET, F. FELDMANN, and N. ROTT, 1946. "Untersuchungen an Verdichtsstössen und Grenzschichten in Schnell Bewegten Gasen", Institut für Aerodynamik, ETH Zürich, *Bericht No.10.*

2. I.E. ALBER, J.W. BACON, B.S. MASSON, and D.J. COLLINS, 1971. "An Experimental Investigation of Turbulent Transonic Viscous-Inviscid Interactions", *AIAA-71-565.*

3. J.M. ALLEN, 1973. "Evaluation of Compressible Flow Preston Tube Calibrations", *NASA TN D-7190.*

4. R. BOHNING and J. ZIEREP, 1973. "Normal Shock-Turbulent Boundary Layer Interaction at a Curved Wall", *AGARD CP-291.*

5. P. BRADSHAW, 1973. "Effects of Streamline Curvature on Turbulent Flow", *Agardograph 169.*

6. J. DÉLERY, 1978. "Analyse du Décollement résultant d'une Interaction Choc-Couche Limite Turbulente en Transonique", *Recherche Aerospatiale 6,* pp. 305-320.

7. G.E. GADD, 1961. "Interactions between Normal Shock Waves and Turbulent Boundary Layers", *ARC R&M 3262.*

8. W. HACKBUSCH, 1985. *"Multigrid Methods and Applications ",* Springer Verlag, Berlin.

9. P.W. HEMKER and S.P. SPEKREIJSE, 1986. "Multiple Grid and Osher's Scheme for the Efficient Solution of the Steady Euler Equations", *Appl. Num. Math. 2,* pp. 475-493.

10. P.W. HEMKER and B. KOREN, 1986. "A Non-linear Multigrid Method for the Steady Euler Equations", *Proceedings of the GAMM-Workshop on the Numerical Solution of Compressible Euler Flows,* Rocquencourt, France, Vieweg Verlag Series Notes on Numerical Fluid Mechanics.

11. G.R. INGER, 1981. "Transonic Shock-Turbulent Boundary Layer Interaction and Incipient Separation on Curved Surfaces", *AIAA-81-1244.*

12. J.W. KOOI, 1975. "Experiments on Shock Wave-Boundary Layer Interaction", *AGARD CP-291.*

13. B. KOREN, 1986. "Euler Flow Solutions for a Transonic Wind Tunnel Section", Centre for Mathematics and Computer Science, Amsterdam, *Report NM-R8601.*

14. B. KOREN, 1987. "Defect Correction and Multigrid for an Efficient and Accurate Computation of Airfoil Flows", to appear in *J. Comp. Phys.*

15. B. KOREN and S.P. SPEKREIJSE, 1987. "An Efficient Solution Method for the Steady Euler Equations", *Proceedings of the Third Copper Mountain Conference on Multigrid Methods,* Copper Mountain, 1987, USA.

16. X. LIU, and L.C. SQUIRE, 1985. "The Shock Wave-Turbulent Boundary Layer Interaction on a Curved Surface at Transonic Speed", *Proceedings of IUTAM Symposium,* Palaiseau, France, Springer Verlag.

17. C. NEBBELING and W.J. BANNINK, 1984. "A Curved Test Section for Research on Transonic Shock Wave-Boundary Layer Interaction", Delft University of Technology, *Report LR-414*.

18. S. OSHER and F. SOLOMON, 1982. "Upwind-Difference Schemes for Hyperbolic Systems of Conservation Laws", *Math. Comp. 38*, pp. 339-374.

19. C. PADOVA, T.J. FALK and C.E. WITTLIFF, 1980. "Experimental Investigation of Similitude Parameters governing Transonic Shock-Boundary Layer Interaction", *AIAA-80-0158*.

20. V.C. PATEL, 1965. "Calibration of the Preston Tube and Limitations on its Use in Pressure Gradients", *J.F.M. 23*, pp. 185-208.

21. W.H. SCHOFIELD, 1983. "Interaction of a Turbulent Boundary Layer with a Normal Shock Followed by an Adverse Pressure Gradient", Defense Science and Technology Organisation, Aeronautical Research Laboratories, Melbourne, *Mechanical Engineering Report 161*.

22. J. SEDDON, 1967. "The Flow produced by Interaction of a Turbulent Boundary Layer with a Normal Shock Wave of Strength sufficient to cause Separation", *ARC R&M 3502*.

23. A. SIGALLA, 1965. "Calibration of Preston Tubes in Supersonic Flow", *AIAA Journal, Vol. 3, No. 8*, pp. 1531.

24. R.J. VIDAL, C.E. WITTLIFF, P.A. CATLIN and B.H. SHEEN, 1973. "Reynolds Number Effects on the Shock Wave-Turbulent Boundary Layer Interaction at Transonic Speeds", *AIAA-73-661*.

25. K.G. WINTER and L. GAUDET, 1970. "Turbulent Boundary Layer Studies at Mach Numbers between 0.2 and 2.8", *RAE TR 70251*.